A Spatially Adjusted Elevation Model in Dronning Maud Land, Antarctica, Based on Differential SAR Interferometry

Reinhard Drews, Wolfgang Rack, *Member, IEEE*, Christine Wesche, and Veit Helm

***Abstract*—In this paper, a new digital elevation model (DEM) is derived for the ice sheet in western Dronning Maud Land, Antarctica. It is based on differential interferometric synthetic aperture radar (SAR) from the European Remote Sensing 1/2 (ERS-1/2) satellites, in combination with ICESat's Geoscience Laser Altimeter System (GLAS). A DEM mosaic is compiled out of 116 scenes from the ERS-1 ice phase in 1994 and the ERS-1/2 tandem mission between 1996 and 1997 with the GLAS data acquired in 2003 that served as ground control. Using three different SAR processors, uncertainties in phase stability and baseline model, resulting in height errors of up to 20 m, are exemplified. Atmospheric influences at the same order of magnitude are demonstrated, and corresponding scenes are excluded. For validation of the DEM mosaic, covering an area of about 130 000 km^2 on a 50-m grid, independent ICESat heights (2004–2007), ground-based kinematic GPS (2005), and airborne laser scanner data (ALS, 2007) are used. Excluding small areas with low phase coherence, the DEM differs in mean and standard deviation by $0.5 +/- 10.1$, $1.1 +/- 6.4$, and $3.1 +/- 4.0$ m from ICESat, GPS, and ALS, respectively. The excluded data points may deviate by more than 50 m. In order to suppress the spatially variable noise below a 5-m threshold, 18% of the DEM area is selectively averaged to a final product at varying horizontal spatial resolution. Apart from mountainous areas, the new DEM outperforms other currently available DEMs and may serve as a benchmark for future elevation models such as from the TanDEM-X mission to spatially monitor ice sheet elevation.**

***Index Terms*—Altimetry, Antarctica, ice sheet elevation, SAR interferometry, SAR processing, synthetic aperture radar (SAR).**

I. Introduction

DIGITAL elevation models (DEMs) of glaciers and ice sheets are used for a variety of applications such as mass balance and accumulation studies [1], input for numerical ice flow models [13], and ice core analysis [22]. For velocity mapping using synthetic aperture radar (SAR) interferometry, an external DEM is necessary to separate the topographic phase from the motion phase in case no suitable coherent repeat pass image pair is available or if the 3-D velocity vector is undetermined [18]. The desirable vertical accuracy and horizontal grid spacing of the DEM is usually application dependent. The required precision in the vertical dimension typically ranges from several meters to submeters. For ice sheet modeling, the typical grid size is several kilometers and comparable to the ice thickness. In order to monitor snow dune migration or grounding line position, a grid spacing of hundreds or tens of meters is needed. Surface elevation over ice sheets is normally measured using satellite altimeters. In the coastal regions of the Antarctic ice sheet, where the surface slope is relatively steep, the performance of conventional radar altimeters is normally poor [4]. ICESat's Geoscience Laser Altimeter System (GLAS) provides surface elevation at higher precision but at sparsely spaced tracks leaving gaps in between [26]. Differential SAR interferometry enables one to fill these gaps using the ICESat data as ground control points (GCPs) [2].

The available Antarctic DEMs are the RAMPv2 model [16], the GLAS model [8], and the JLB97 model [3], which are gridded at 200 m, 500 m, and 5 km, respectively. The second version of the RAMP model originates from the Radarsat Antarctic Mapping Project and is deduced from European Remote Sensing 1 (ERS-1) satellite radar altimetry in the flat central parts of the ice sheet. In areas with steep relief, it is combined with data from the Antarctic Digital Database (4.0), photogrammetry, airborne radar surveys, and ground-based data like GPS measurements. JLB97 is based on ERS-1 radar altimetry as well [4]. The GLAS model is interpolated from ICESat's laser altimeter heights and was released from the National Snow and Ice Data Center (NSIDC) in 2007. In our area of interest, all data sets exhibit deviations when compared with each other, as well as when compared to ground-based data (see Section III-C).

Satellite-borne interferometric SAR (InSAR) is a well-known technique to derive area-wide fine-resolution DEMs and velocity fields. Detailed descriptions can be found, for example, in [10], [17], or [21]. Studies with respect to ice sheet elevation were previously performed in [2], [14], or [15]. Our study area is a 1.3×10^5-km^2-wide section of the grounded ice sheet in the Atlantic sector of Antarctica (Fig. 1). The surface elevation rises from about 100 m a.s.l. near the grounding line to about 2500 m south of the Heimefrontfjella mountain range. The typical surface slope is 0.5°. The main ice streams draining this area are the Stancomb Wills and Veststraumen in the west and smaller ice streams flowing toward the Ekström and Fimbul ice shelves in the east. Ice velocities reach up to 1 m/day. Comparable high ice velocities are also observed at glaciers in

Manuscript received April 26, 2008; revised September 17, 2008 and January 19, 2009. The work of R. Drews was supported by the Evangelisches Studienwerk Villigst.

R. Drews, C. Wesche, and V. Helm are with the Alfred Wegener Institute for Polar and Marine Research, 27515 Bremerhaven, Germany (e-mail: reinhard.drews@awi.de).

W. Rack is with the Gateway Antarctica Centre for Antarctic Studies and Research, University of Canterbury, Christchurch 8140, New Zealand.

Color versions of one or more of the figures in this paper are available online at http://ieeexplore.ieee.org.

Digital Object Identifier 10.1109/TGRS.2009.2016081

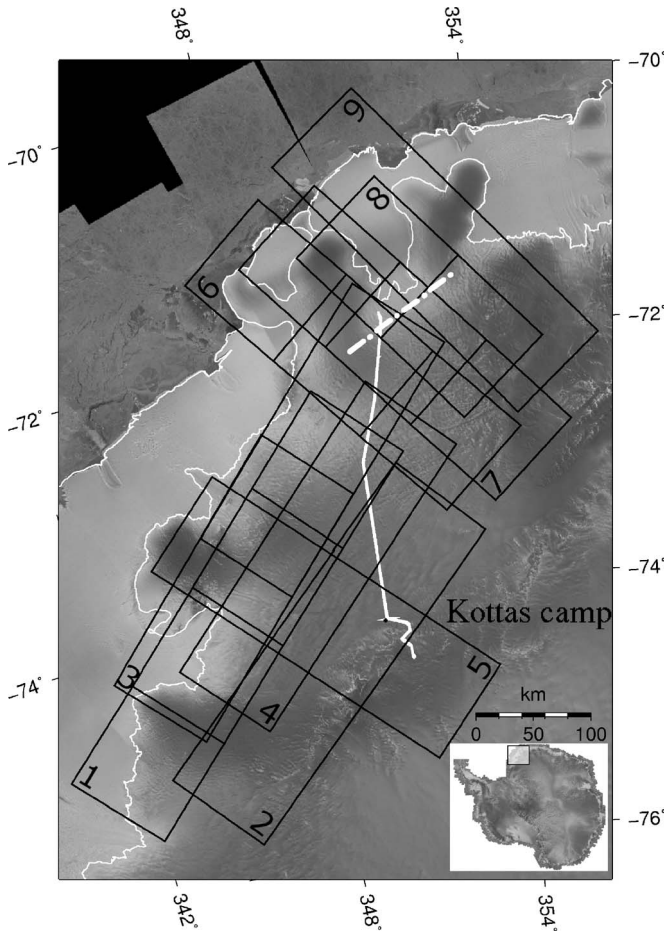

Fig. 1. Radarsat image mosaic of Dronning Maud Land showing used ERS satellite frames, together with the GPS traverse between (white bold line) the Ekström Ice Shelf and the Kottas camp, and (white dashed line) the ALS profile. The fine white line delineates the floating ice shelves.

the vicinity of the Heimefrontfjella mountains. Ice dynamics and data from repeat pass interferometers require a differential InSAR approach in order to cancel out ice velocity and to derive DEMs.

Baek *et al.* [2] reported localized residual elevation discrepancies between their DInSAR DEMs and ICESat altimetry. They speculated on the origins such as variable atmospheric path delays and varying radar penetration depths into snow. Our interest is to derive a larger scale DEM using the same technique, quantify the obtainable accuracy, and link deviations to two kinds of errors: first, internal errors due to uncertainties within the SAR/InSAR processing, and second, external errors such as an atmospheric contribution due to variable path delays. Finally, we present a DEM with a varying horizontal resolution that accounts for the spatial variation of noise.

II. Methodology

In an interferometric multipass procedure, two SAR acquisitions are combined to derive a mixed interferogram that contains a topographical contribution and an additional contribution due to the ice displacement between data acquisitions. In order to separate these two parameters, a differential approach (DInSAR), as described in [15], is chosen. Under the assumption of a constant ice flow, the displacement

TABLE I
Overview of ERS Satellite Frames and Tracks, Acquisition Date, and Differential Perpendicular Baseline. ID Refers to Track Numbers in Fig. 1

id	track	frame	date	$\bar{B}_\perp$ (m)	orbit
1	450	5139-5193	2/3 Nov-23/24 Mar 95/96	67	descend.
2	35	5157-5193	12/15/18 Mar 94	101	descend.
3	221	5103-5139	5/6 Mar-9/10 Apr 1996	233	descend.
3	221	5157-5175	17/18 Oct-9/10 Apr 95/96	86	descend.
4	407	5139-5175	30/31 Oct-18/19 Mar 95/96	235	descend.
5	17	5607-5643	14/17/20 Mar 94	27	ascend.
6	31	5661-5697	06/09/12 Mar 1994	81	ascend.
7	45	5661-5679	22/23 Mar-13/14 Mar 96/97	193	ascend.
8	2	5679	15/16 Jan-19/20 Feb 1996	230	ascend.
9	460	5679-5715	16/17 Feb-22/23 Mar 96	159	ascend.

is canceled by subtracting two interferograms of the same scene. The main processing steps comprise the SAR processing of the raw data, coregistration of the scenes, interferogram formation, phase unwrapping, subtraction of the interferograms, baseline refinement, and georeferencing to the resulting height map. As previously done in [2], the baseline refinement uses GCPs from ICESat's laser altimeter (GLA 12 Release 24, Laser 1 (20.02.2002–29.03.2003) and Laser 2a (24.09.2003–18.11.2003) [26]), which provides a tie point every 170 m along the satellite track (see also Section III-C).

Limitations are, for example, the restricted availability of coherent SAR image pairs, a change in surface height or slope between the ICESat and SAR acquisition, and the lack or uneven distribution of GCPs. Variable atmospheric path delays [10], as well as varying radar penetration into snow [19], may also deteriorate the quality of the resulting DEM. It is also possible that the ice flow changes between the InSAR image pair acquisition and thus does not fully cancel in the DInSAR approach.

We investigate the robustness and sensitivity of the SAR raw-data processing by analyzing data from three different SAR processors with varying scene length in azimuth. Some DEMs were derived from single-look complex (SLC) frames from the German Processing and Archiving Facility (D-PAF; processing date between 2003 and 2007). The resulting DEMs often show phase discontinuities on the border of adjacent frames, which cannot be fully explained by baseline inaccuracies. In order to enable strip-line processing, we used Gamma's Modular SAR Processor (MSP) and, for comparison, EarthView's Advanced Precision Processor (APP). All other steps were performed with Gamma's interferometry software [24].

Fig. 1 and Table I display the ERS frames that were used in this paper. Altogether, 19 DEMs were separately derived and mosaicked to a final DEM. Ascending and descending orbits were handled equally as no biases have been observed.

In overlapping areas, individual DEMs were stacked by applying a weighted average in order to reduce data noise. The weights were given by the differential perpendicular baseline $\mathbf{b}_\perp^{\mathbf{k}}$ of the respective DEM and by the coherence $cc_{i,j}$ for each pixel. The coherence was estimated after applying an adaptive fringe filter to the differential interferogram [9]. For the sake of simplicity, we assumed a linear dependence of weights. In detail

$$\mathrm{DEM}_{(i,j)} = \frac{\sum_{k,k'=1}^{N} cc_{(i,j)}^{k} b_\perp^{k'} \mathrm{dem}_{(i,j)}^{k'}}{\sum_{k,k'=1}^{N} cc_{(i,j)}^{k} b_\perp^{k'}} \qquad (1)$$

with

$$cc_{i,j}^{k} = \begin{cases} cc_{i,j}^{k}, & \text{if } cc_{i,j}^{k} > 0.6 \\ 0, & \text{otherwise} \end{cases}$$

where k and k' index the individual DEMs and N is the number of DEMs that overlap at the location (i, j). Usually, N is between two and four. In the case of $N > 1$, the threshold for coherence was chosen to avoid areas of high noise that tend to deteriorate the quality of the final DEM when compared to independent GCPs.

For the uncertainty estimation, the final DEM is compared to ICESat tracks, as well as independent GPS and airborne laser scanner data in Section III-C. The submeter accuracy of these data sets permits a detailed comparison with the DInSAR DEM along the profiles. However, it does not evaluate the DEM area-wide.

Fig. 1 shows that many individual DEMs overlap with each other. This enables not only stacking but also subtraction in common areas. The latter results in an area-wide quality map [see Fig. 7(a)]. It indicates error boundaries of height deviations that can be caused by an interplay of various error sources (e.g., atmospheric contribution, varying penetration depth, changing ice flow, and imprecise processing).

Processing uncertainties alone can be visualized when overlapping raw data are processed individually. This is done for the small overlap of adjacent frames from the same data track and will be discussed in more detail in the following section.

III. Accuracy Analysis

A. SAR Raw-Data and DInSAR Processing

SAR raw-data processing aims to reconstruct an image out of several backscattered pulses by using the Doppler history of the individual targets [7], [11]. The resulting full-resolution image is an SLC file that stores a complex number (in-phase and quadrature) from which phase and amplitude can be derived. After the double subtraction of four SLCs, the conversion from differential phase to height can be approximated by [20]

$$z = \frac{\lambda r \sin(\theta)}{4\pi} \frac{\Delta\phi_f}{B_\perp} \tag{2}$$

where the unwrapped and flattened phase ϕ_f is turned into height z (above a reference ellipsoid) by using the perpendicular component of the refined baseline B, as well as the look angle θ, the slant range distance r, and the wavelength λ. Apart from the wavelength, all parameters have a range and azimuth dependence that is not marked explicitly.

Processing uncertainties can be visualized through the following ways: 1) comparing overlapping areas of adjacent frames that were processed individually; 2) comparing DEMs that are based on a set of SLCs originating from different SAR processors; or 3) generating autointerferograms (interferograms generated from the identical scene with different SAR processing history). In all cases, the resulting DEMs rely on the same raw data, and deviations can be entirely attributed to processing.

As a specific example, we consider two adjacent frames (5157 and 5175) in track 407 that is marked with 4 in Fig. 1.

TABLE II
Comparison of ICESAT GCPS to DEMS of Satellite Track 407 Derived From SLCS Originating From Different SAR Processors

DEM identifier	SAR Processor	frame number	deviation s_{Ice} to ICESat GCPs [m]
D1	D-PAF	5157	-0.3 ± 3.1
D2	D-PAF	5175	-0.4 ± 7.0
Ev1	APP	5157	0.3 ± 2.0
Ev2	APP	5175	0.4 ± 5.1
G	MSP	5157-5175	0.0 ± 3.7

From this raw-data strip, we derived five DEMs (D1, D2, Ev1, Ev2, and G), which are listed in Table II.

D1 and D2 are based on eight SLCs from the German D-PAF, and Ev1 and Ev2 are based on eight SLCs from EarthView's APP. G is based on four SLCs from the MSP where the raw data of the two frames have been concatenated. In order to investigate differences between the five DEMs, we first compare the deviations to the GCPs from the baseline refinement and then compare the DEMs with each other. The deviations are eventually traced back to differences in the baseline models and the SAR processing history of the individual SLCs.

The comparison of ICESat GCPs with the corresponding DEMs is summarized in Table II. In all cases, the deviation s_{Ice} scatters around zero with a standard deviation of 2–7 m. Many long ICESat tracks show random deviations from 1 to 2 m, which points out the generally high quality of those particular DEMs. However, in some regions, the deviations are systematic and reach up to 10 and 15 m. This is shown in Fig. 2 for D1, D2, and G. Characteristic dents are particularly visible in the upper right and lower left corners of D2 (Fig. 2, upper left frame, marked with arrows). These dents cover areas of up to 20 km in length and are evident in many DEMs. They cannot be removed with low-order polynomials in a global fit over an entire frame. It is important to know whether these localized deviations have geophysical reasons or if they are due to processing. In our case, many of them are due to processing since, depending on which set of SLCs has been used, they appear in different places. This can be seen in Fig. 2 where the previously mentioned dents from D2 are not visible in G.

The difference fields of D1, Ev1, and G, as well as the difference fields of D2, Ev2, and G, show deviations of up to 15 m in some areas. Similar deviations can also be seen in the overlapping area of D1 and D2. This emphasizes that most of the localized deviations along the ICESat tracks are processing artifacts. The magnitude of processing uncertainties can be explained with deviations in the differential phase and baseline models. The typical InSAR approach for the baseline model is to account for inaccuracies in the state vectors with an overall fit of GCPs to the unwrapped differential phase. This alters the baseline in a way that the resulting orbit model complies best to the used set of GCPs. For D1 and D2 (adjacent frames from the same track), a different set of GCPs for each frame is used. This leads to a discontinuity in the baseline model within the common raw data of the two frames and eventually causes a height difference in the overlapping area of the corresponding DEMs. However, height differences remain even if the two baseline models are artificially merged. This is due to additional deviations in the differential phase which originate from the SAR processing history of the individual

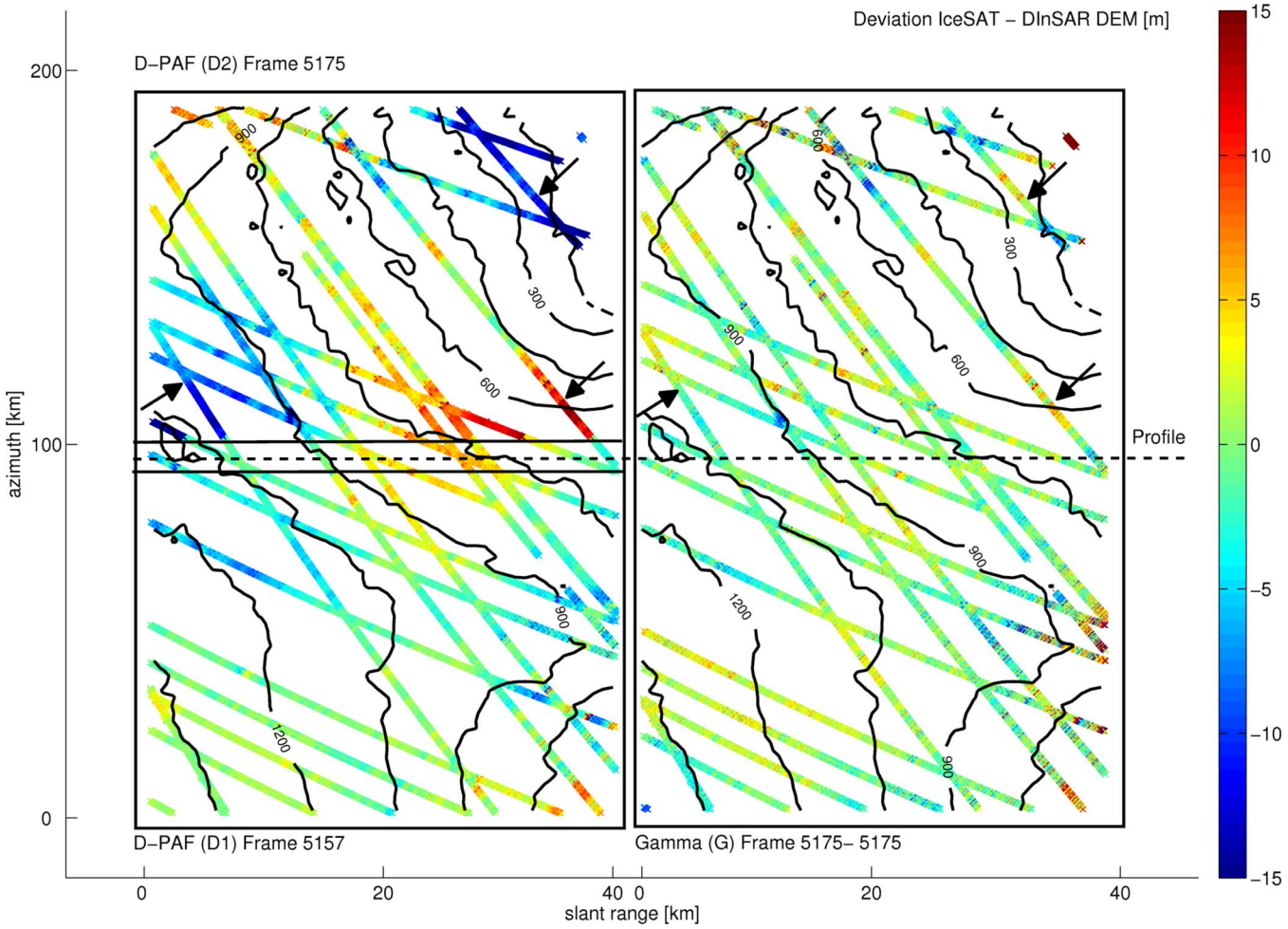

Fig. 2. Comparison of ICESat GCPs with DEMs based on SLCs with different SAR processing histories (D1, D2, and G). Localized elevation discrepancies (dents) of up to 15 m along the ICESat tracks appear as (marked with arrows) processing artifacts in the lower left and the upper right corner of D2. The same dents do not appear in G. The dashed line indicates the profile where D1, D2, and G are compared with each other (see Fig. 3).

SLCs. For D1 and D2, deviations in phase become visible in the form of discontinuities when the single flattened interferograms are appended. In the case of D1 and Ev1, as well as D2 and Ev2, the residual phase can be visualized via autointerferograms that display the phase differences of individually processed SLCs from the common raw data [5]. Autointerferograms with G are overlaid with a phase ramp of several fringes because MSP SLCs are not processed to a zero-Doppler geometry and are thus not directly comparable to APP and D-PAF SLCs.

Fig. 3 exemplifies the deviations in differential phase, differential baseline, and height along a range profile (shown in Fig. 2) that intersects D1, D2, Ev2, and G. It becomes evident that the various DEMs are tilted with respect to each other. The largest tilts can be seen in the pairs D2–G and D2–D1. Similar results are obtained for the case that the two frames in G are processed separately.

In order to evaluate the influence of the observed deviations in the baseline model and differential phase, we use (2) and approximate the expected height difference $z - z'$ with

$$z - z' = \frac{\lambda r \sin\Theta}{4\pi} \cdot \left(\frac{\Delta\phi_f B'_\perp - \Delta\phi'_f B_\perp}{B'_\perp B_\perp} \right). \qquad (3)$$

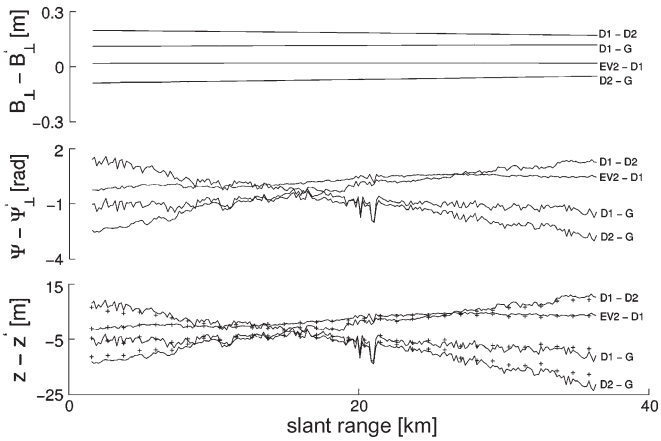

Fig. 3. Comparison of differential perpendicular baseline $B_\perp$, differential phase ϕ, and height z for a profile in the range within the overlapping areas of independently processed DEMs (D1 and D2 with D-PAF, Ev1 with EarthView, and G with MSP). The + symbols in the lowest plot mark the predicted height deviation according to (3). The profiles are gridded to a 160-m raster.

The + symbols in the lowest plot of Fig. 3 indicate that this analytical deviation predicts the observed height deviation well. It supports the idea that differences in the baseline model and phase are, in fact, the main parameters for the deviation.

We can only speculate about the origin of deviations in phase, as the exact implementation of the SAR processors is unknown. Some parameters are estimated by the SAR processors for each individual frame. This can cause phase discontinuities on the borders even if the same SAR processor has been used. One such parameter is the estimation of the Doppler centroid and its range dependence. For the latter, the D-PAF SLCs are usually based on a quadratic function, whereas the MSP's representation tends to be linear. Using the MSP, the low contrast within the scenes often excludes the use of an iterative autofocus routine to adjust the Doppler ambiguity number, and larger squint angles in the Southern Hemisphere aggravate the processing of scenes over Antarctica [24]. In the case of G, we processed the SLC pairs to a common Doppler for maximum spectral overlap. What is seen in Fig. 3 as the deviation in differential phase is the summation of tilts from the individual SLCs.

It should be noted that, in other examples, the differences in similar comparisons did not show any tilts in phase, and height differences seldom exceeded 1 m. Also, a comparison with independent GCPs, which is shown in Section III-C, points to a higher accuracy in other areas of the DEM.

We globally adjusted each individual DEM with a third-order polynomial to GCPs, which generally improves the DEM quality and diminishes differences in overlapping areas. However, in only a few cases, it is possible to completely remove processing dents using polynomial fits.

B. Atmospheric Contribution

Variations in tropospheric water vapor content are a source of lateral inhomogeneities in refractivity [10], [25] that is often neglected for the comparatively dry polar atmosphere. This is shown in Fig. 4 showing a residual DEM that was derived from frame 5661 of tracks 31 and 45. The mean elevation of that area is 1800 m. Track 31 was recorded several times in March 1994 (ERS-1 ice phase), and track 45 is a combination from interferograms of 1996 and 1997. A wavelike pattern with an amplitude of about 20 m and a wavelength of about 10 km can be seen in the difference field. In this obvious case, the pattern can be recognized in single interferograms from track 31 (March 9–12 and 12–15, 1994). It is traced back to the data acquisition of March 12, 1994, 1:40 UTC. A NOAA AVHRR satellite image (March 11, 1994, 23:17 UTC) shows a dominant high cloud band in the area of the image frame, which is related to a low-pressure system, with its center being located off the coast of Antarctica at about 12° W/68° S (24-h polar MM5 reanalysis forecast, Byrd Polar Research Center). It causes a strong southeasterly flow over the Heimefrontfjella mountain range. Wavelike structures in the AVHRR image with similar spatial scales cannot be spotted exactly in the area of the ERS SAR image but in the area to the northwest. This is probably because of the 2-h time difference in data acquisition between the AVHRR and the SAR image. Temperature differences indicate a close sequence of high and low clouds with significant differences in water vapor content and precipitable water. Taking into account the (differential) baseline, the observed wave amplitude in Fig. 4 corresponds to a maximum path delay of 9 mm in the March 12 SAR image.

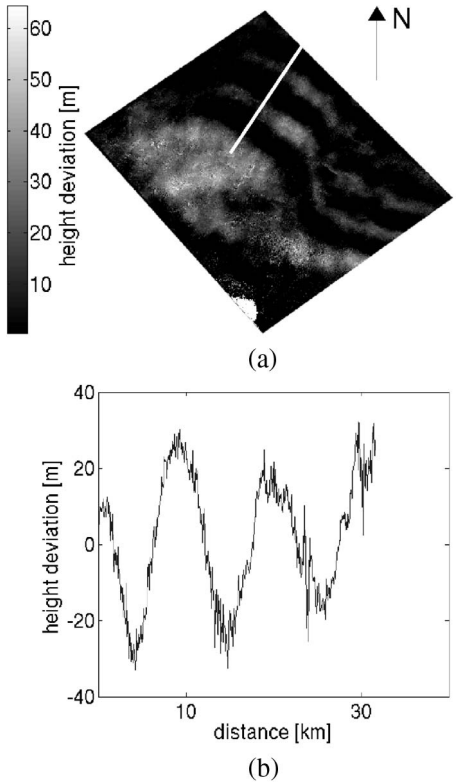

Fig. 4. (a) Difference field of DEMs from track 31 (1994) and track 45 (1996/1997) of frame 5661. (b) (Marked as white line) Profile across the wavelike structure.

This particular frame and obvious case was not considered for our final DEM product, but it is a showcase that, in general, atmospheric inhomogeneities could be too large to be neglected, particularly for small baselines. Because the database for differential interferograms in this area is limited, we cannot assume that atmospheric contributions due to changes in path delay are completely canceled out by the stacking procedure in (1).

C. DEM Validation Against Satellite, Air, and Ground Data

We compare our DInSAR DEM, as well as the RAMPv2, JBL97, and GLAS models, to GCPs from additional ICESat tracks, kinematic GPS, and airborne laser altimetry. In the case of the DInSAR DEM, the comparison with ICESat tracks is flawed as data from similar tracks are used for the baseline refinement. However, a comparison yields two aspects. First, in areas of low coherence, the standard deviation toward ICESat increases and indicates the effect of coherence on the DEM's quality. Second, the appearance of local dents, as described in Section III-A, can be visualized along the ICESat tracks over longer distances. Entirely independent are the GPS and ALS profiles that run in between the ICESat tracks. The characteristics of the individual GCP data sets are as follows.

The ICESat tracks for the validation include data from GLA12 Release 28 (L3b–L3h), which were recorded in 2004–2007 [27]. The height error of the ICESat laser altimetry, as given in [6], varies between 14 to 59 cm as a function of surface slope. We performed a crossover analysis for each period in our area of interest and found a mean absolute

elevation difference of 80 cm. These higher deviations can be caused by a combination of steeper surface slope and stronger accumulation variability (e.g., due to snow drift) compared to the Antarctic plateau. The deviations in crossover points within the individual laser periods aggravate a change detection between the different laser periods. In the latter, we see elevation differences, particularly near the coast, but these usually do not exceed 1 m. Compared to our DEM, these values do not represent a systematic change in surface elevation. Therefore, we combine all laser periods for further comparison.

The laser altimetry survey took place in December 2007 and was similar to that described in [12]. The airborne laser scanner (ALS) was installed onboard of the Polar5, the new scientific aircraft of the Alfred Wegener Institute. The position of a 115-km-long profile is shown in Fig. 1. Apart from the ALS (Riegl LMS-Q280), the instrumentation included a Honeywell inertial navigation system (INS), four GPS receivers, and an airborne SAR interferometric radar altimeter system. The ALS was operated at 80 Hz with a scan angle of 45°. The average flight altitude of 700 m above ground, together with an average ground speed of 67 m/s, results in an ALS footprint separation of about 1 m along and 6 m across track. The ground stations at the South African base SANAE IV (Vesleskarvet) (2.84° W and 71.67° S) and the Russian base Novolazarevskaya (11.83° E and 70.77° S) served as references for the differential GPS postprocessing. The geocoded ALS heights were determined using the postprocessed GPS, INS, and calibrated ALS range measurements. The performance of the system is equal to that in the Greenland survey [12], and the preliminary overall ALS height accuracy (including the GPS height uncertainty) is estimated to be at the submeter level.

The approximately 300-km-long GPS traverse shown in Fig. 1 is located on grounded ice between the Ekström Ice Shelf and the Kottas mountains. Data were collected in December 2005, with the GPS antenna mounted on top of a dragged living container. A recording interval of 1 s, together with a typical travel speed of 10 km/h, results in a height recording about every 3 m. The GPS data were processed with a commercial postprocessing software, including reference stations, precise ephemerides, and ionospheric-free solutions. Vesleskarvet and the Finnish station Aboa (13.41° W and 73.04° S) served as reference stations. Due to the local recording intervals of 30 and 15 s, the reference data were interpolated to 1-s intervals by using the INTERPO software from the National Geodetic Survey. Since no crossover points are available, the statistics are taken from the processing report of the software. It is estimated that all data points have a standard deviation of less than 1 m.

In order to compare the GCP data with the individual DEMs, GCPs are averaged to the respective cell sizes of the DInSAR, RAMPv2, GLAS, and JLB97 models. The comparison shows the largest differences at the steep incline near the Heimefrontfjella mountain range. Compared to the GPS traverse in that area, the DInSAR, RAMPv2, and JLB97 models show strong deviations of more than 50 m. In both cases, this error is slope-induced with the additional effect of low coherence in the DInSAR data. GLAS shows smaller deviations. For further analysis, we excluded that area and filtered the complete DInSAR DEM with a (postprocessing) coherence threshold of 0.8. This precluded about 15% of the ICESat points and less than 10% of the GPS and ALS points. The results are summarized in Table III and stated as the mean difference ± 1 standard deviation. If no coherence filter is applied, some point-to-point comparisons deviate by more than 50 m. However, this is only the case for a minor part of the complete DInSAR DEM.

TABLE III
MEAN AND STANDARD DEVIATION OF DEMS MINUS GCPS FROM GPS, ICESAT, AND ALS. FOR THE COMPARISON WITH THE DINSAR DEM, GCPS WERE FILTERED WITH A POSTPROCESSING COHERENCE THRESHOLD OF 0.8 (EXCLUDED $< 15\%$ OF ICESAT GCPS AND $< 10\%$ OF ALS AND GPS GCPS). THE GPS, ALS, AND ICESAT DATA WERE COLLECTED IN 2005, 2007, AND 2004–2007, RESPECTIVELY

-	GPS [m]	ALS [m]	ICESat [m]
DInSAR 50x50m	-1.1 ± 6.4	-3.1 ± 4.0	-0.5 ± 10.1
RAMPv2 200x200m	33.7 ± 85.6	96.6 ± 47.1	6.8 ± 27.0
GLAS/ICESat 500x500m	1.1 ± 6.9	2.4 ± 11.5	-0.2 ± 4.5
JLB97 5x5km	-4.2 ± 11.7	-3.0 ± 22.5	-5.4 ± 17.4

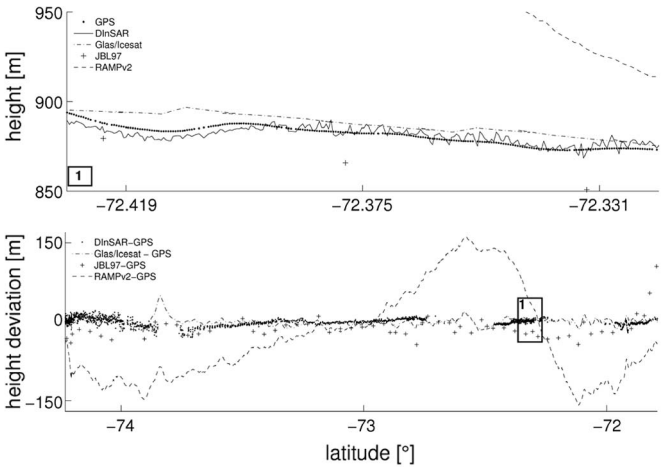

Fig. 5. Comparison of DInSAR (50 m × 50 m), GLAS (500 m × 500 m), RAMPv2 (200 m × 200 m), and JLB97 (5 km × 5 km) with the 300-km-long GPS traverse on grounded ice between the Neumayer base and Kottas camp. The bottom plot displays the deviations from the sampled GPS heights to the grid points of the respective DEM. The top plot is a zoom to the absolute heights marked as box 1. The DInSAR heights were filtered with a postprocessing coherence threshold of 0.8 that excluded less than 10% of the data.

The comparison with the GPS traverse is exemplified in Fig. 5 and shows that RAMPv2 exhibits the largest differences that reach up to 150 m. The standard deviation GPS to JLB97 is about 12 m, whereas GPS to GLAS and DInSAR have standard deviations between 6 and 7 m. Compared to DInSAR, GLAS is smoother but does not show undulations in the kilometer scale that are as detailed as that of DInSAR.

The DInSAR data reveal the smallest standard deviation (4.0 m) of all DEMs when compared to the ALS data. The relatively large offset of -3.1 m may be caused by a local variation in surface height over time since local snow accumulation is around 1 m/a [22]. The ALS data were recorded in December 2007, whereas the DInSAR DEM data in this area were from February 1996.

The ICESat tracks are evenly distributed over the entire DInSAR DEM [see Fig. 7(c)]. For comparison, we further excluded outliers ($\sim$0.01%) with deviations larger than 50 m, which are mostly caused by hidden phase unwrapping errors. This is most likely in isolated areas where the surrounding

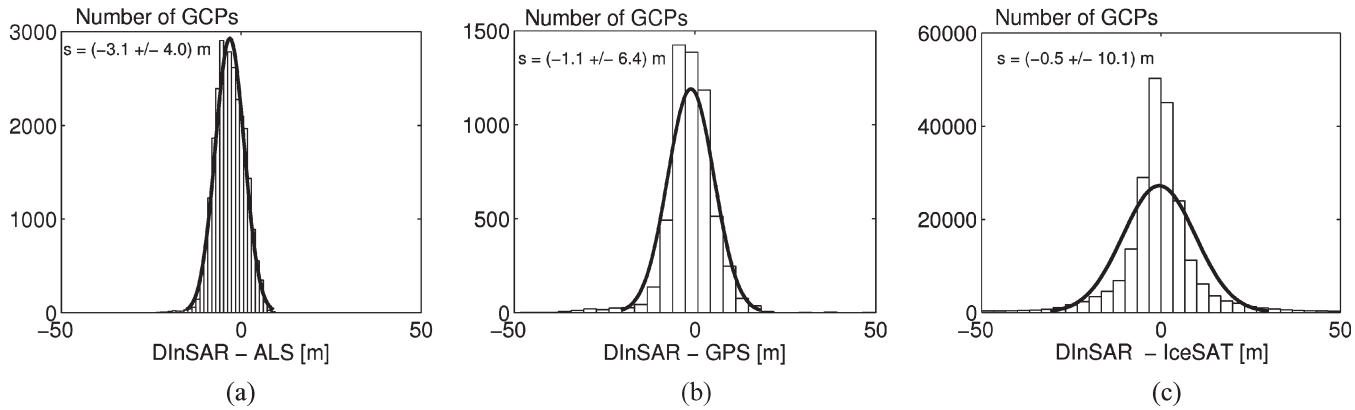

Fig. 6. Histogram of the DInSAR DEM compared to (a) ALS, (b) GPS, and (c) ICESat GCPs. GCPs were filtered with a postprocessing coherence threshold of 0.8 (excluded $< 15\%$ of ICESat GCPs and $< 10\%$ of ALS and GPS GCPs). The black line represents the corresponding Gaussian distribution.

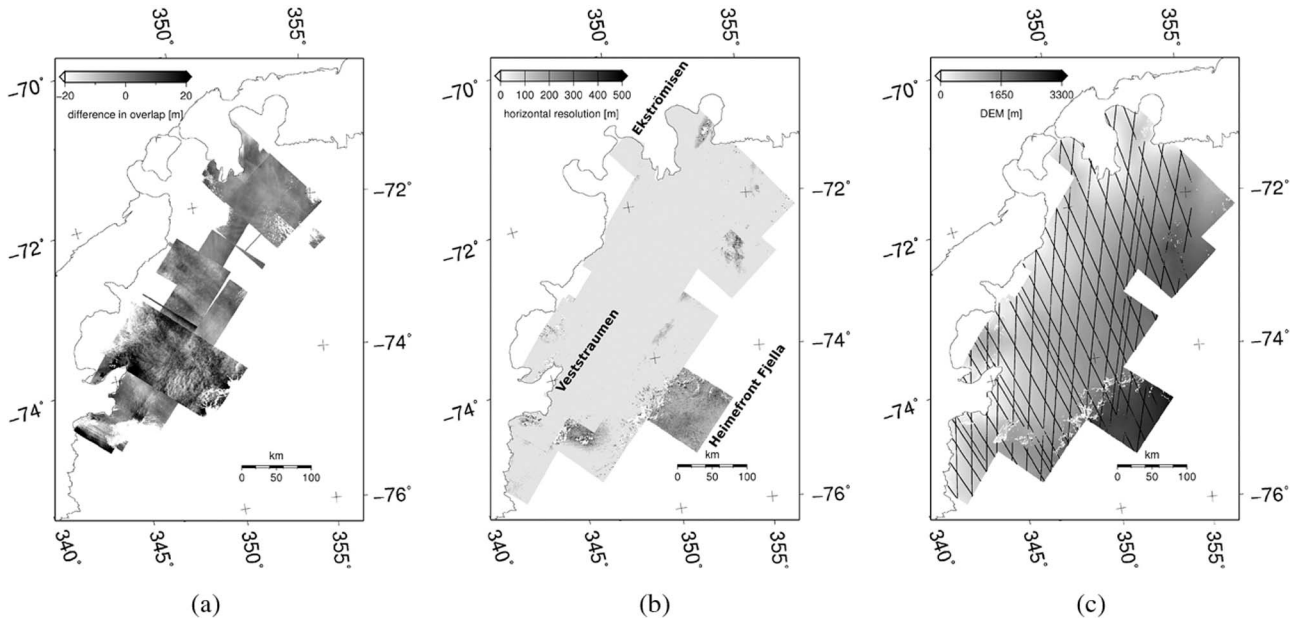

Fig. 7. (a) Mean difference field of DEMs in overlapping areas. (b) Horizontal resolution after iterative averaging. Areas with lower horizontal resolution than 250 m typically mark the areas where the DEM shows deviation larger than 50 m when compared to independent GCPs. The resampled DEM is shown in (c) where areas with a standard deviation higher than 5 m are masked out. ICESat tracks that were used for the baseline refinement are overlaid with black lines.

was masked out during processing because of low coherence. In general, the deviations to ICESat points in areas of high (postprocessing) coherence (> 0.9) are below 2 m, whereas in areas of lower coherence, the deviations increase to 20 m. The overall standard deviation is 10.1 m. With a standard deviation of about 5 m, the GLAS model naturally performs best in the vicinity of the ICESat tracks as the interpolated DEM is based on the ICESat data. JLB97 and RAMPv2 show standard deviations of about 17 and 30 m, respectively.

Localized deviations similar to those marked in Fig. 2 are still evident in the mosaicked DInSAR DEM, also when compared to the ALS or GPS data. Most of them probably originate from residual processing errors, as discussed in Section III-A. Overall, along the GPS and ICESat profiles, the deviations do not follow a Gaussian distribution, which is shown in Fig. 6. This is because these profiles also cover areas where the DEM mosaic is based on individual DEMs with lower coherence, which results in increased scattering and longer tails in the positive and negative domains. This is not the case with the ALS profile where coherence is high without exception and deviations are Gaussian. This demonstrates that, despite the weighting procedure in (1), coherence is still the important driver for the spatial variation of quality in the DInSAR DEM. This will be accounted for in the next section.

IV. Spatial Variation of Quality in Surface Elevation

Two maps indicate the spatial variation of vertical accuracy in the DInSAR DEM: the mean difference field in the overlapping areas of all frames and the mean coherence map of the entire DEM. The difference field is shown in Fig. 7(a). It illustrates height differences that can be caused by a variety of reasons, for example, processing artifacts, atmospheric contribution, varying penetration depth, or slope-induced errors. Apart from the previously mentioned examples in

Section III-A and B, the individual error sources cannot be easily distinguished. The coherence map marks areas with low coherence, where increased phase noise leads to deteriorating surface heights. This can be accounted for by iteratively applying an adaptive low-pass filter. Averaging with a factor of $n \times n$ decreases the standard deviation by a factor of n at the cost of spatial resolution. We chose a simple algorithm to resample the DEM, iteratively lowering the local standard deviation below a threshold of 5 m. In the first step, the standard deviation is estimated on the 50-m grid in flattened 750 m $\times$ 750 m windows. If the standard deviation is below the threshold, the subwindow is excluded; otherwise, the DEM is resampled with a 50-m increment up to a maximum cell size of 500 m. This results in a DEM with a varying spatial resolution, which is shown in Fig. 7(b). In particular, areas with steep relief near the Heimefrontfjella mountain range and some coastal areas needed higher filtering or were completely masked out. After the filtering, 82% of the DEM stayed on the 50-m grid.

V. Summary and Conclusion

In this paper, 19 independent DEMs were derived by applying a differential interferometric approach. The DEMs are based on the SAR data from ERS-1/2, in combination with laser altimetry from ICESat. The SAR data were acquired in ERS-1's ice phase in 1994 and during the ERS-1/2 tandem mission from 1996 to 1997. The altimeter data were recorded in 2003. The mosaicked DEM covers an area of approximately 1.3×10^5 km^2. The overlapping parts of adjacent frames and autointerferograms were used to separate different error sources. In that process, a cross-comparison was performed between DEMs, which are based on the same raw data but on different SLC products. It has been demonstrated that processing uncertainties are not always negligible and often depend on the processing history of the used set of SLCs. From a software end-user perspective, it is difficult to evaluate and adjust possible inaccuracies originating in the raw data to SLC processing, which may superimpose other geophysical effects. If only one frame with a single set of SLCs is available, unnoticed processing uncertainties could potentially overlay effects such as varying penetration depth. In [23], the penetration depth for dry snow in the same study area was estimated to be on the order of 22 m using a C-band frequency scatterometer. However, the observed dents shown in Fig. 2 are of the same order of magnitude, and a variation in penetration depth between adjacent snow regimes is likely to be smaller. Although strip-line processing removes discontinuities between frame boundaries, it does not necessarily raise the overall accuracy.

A comparison with an approximately 300-km-long GPS traverse from 2005 on the 50-m grid reveals a deviation of $s_{\mathrm{GPS}} = (-1.1 \pm 6.4)$ m. The deviation to the laser altimetry profile from 2007 is $s_{\mathrm{ALS}} = (-3.1 \pm 4.0)$ m, and deviations toward ICESat GCPs from 2004–2007 are $s_{\mathrm{Ice}} = (-0.5 \pm 10.1)$ m. In all cases, DInSAR points with a postprocessing coherence lower than 0.8 have been excluded. Some of these excluded points show deviations larger than 50 m. The comparison with ICESat GCPs alone does not entirely reflect the DEM's accuracy: first, because they were used to refine the baseline, and second, because the comparison is only along profiles and not area-wide. In areas where different frames with high coherence could be stacked, the DEM shows typical deviations to GCPs below 2 m. In areas with lower coherence, the typical deviation increases to 20 m.

Apart from the atmospheric disturbances that were discussed in Section III-B and removed from the data set, no other atmospheric influences are obvious in the difference field of the DEM. The overall phase coherence is high (> 0.9, as estimated from the fringe filtering algorithm), and also, areas of lower coherence (< 0.7) are well mapped. In order to attenuate contributions from processing artifacts and variations in atmospheric path delay, we applied a stacking procedure, including DEMs originating from interferograms with comparable low phase coherence. The resulting DEM was iteratively low-pass filtered with a spatially varying kernel size to lower the standard deviation in a predefined window below a 5-m threshold. In this procedure, 82% of the final DEM remained on a 50-m grid. Areas with lower horizontal resolution than 250 m typically mark the areas where the DEM shows deviation larger than 50 m when compared to independent GCPs.

A difference field of heights from individual DEMs was generated and serves as an indicator for the spatial variation of the DEM quality. Other DEMs in that region (RAMPv2, GLAS, and JLB97) are lesser resolved and show larger differences to the validation data. Overall, our new DInSAR DEM can be considered to have good vertical precision and the best horizontal (50 m $\times$ 50 m) resolution currently available in that region.

Acknowledgment

The authors would like to thank C. Werner (Gamma Remote Sensing) for the help during the SAR processing; M. Bässler (TU Dresden) for the provision of the sample data; and H. Koivula and J. Mäkinen (Finnish Geodetic Institute) for providing the GPS reference data. The authors would also like to thank Gateway Antarctica for enabling a six-month internship for R. Drews. The comments of the three anonymous reviewers significantly improved this paper. The ERS SAR data were made available by ESA through Project AO3108. The ALS data were acquired for DLR Project 50EE0505. The ICESat, RAMP, and AVHRR satellite data were provided through NSIDC. The MM5 reanalysis data were provided by D. Steinhoff, Polar Meteorology Group, Byrd Polar Research Center.

References

[1] H. Anschütz, O. Eisen, H. Oerter, D. Steinhage, and M. Scheinert, "Investigating small-scale variations of the recent accumulation rate in coastal Dronning Maud Land, East Antarctica," *Ann. Glaciol.*, vol. 46, no. 1, pp. 14–21, Oct. 2007.

[2] S. Baek, O. Kwoun, A. Braun, L. Zhong, and C. Shum, "Digital elevation model of King Edward VII Peninsula, West Antarctica, from SAR interferometry and ICESat laser altimetry," *IEEE Geosci. Remote Sens. Lett.*, vol. 2, no. 4, pp. 413–417, Oct. 2005.

[3] J. Bamber and R. Bindschadler, "An improved elevation dataset for climate and ice-sheet modelling: Validation with satellite imagery," *Ann. Glaciol.*, vol. 25, pp. 438–444, 2001.

[4] J. Bamber and J. Gomez-Dans, "The accuracy of digital elevation models of the Antarctic continent," *Earth Planet. Sci. Lett.*, vol. 237, no. 3/4, pp. 516–523, Sep. 2005.
[5] A. Barmettler, P. Pasquali, D. Small, and D. Nuesch, "Cross-compatibility of ERS-SLC products," in *Proc. 2nd Workshop FRINGE SAR Interferometry Working Group*, Zürich, Switzerland, Oct. 1996, p. 309.
[6] A. C. Brenner, J. P. DiMarzio, and H. J. Zwally, "Precision and accuracy of satellite radar and laser altimeter data over the continental ice sheets," *IEEE Trans. Geosci. Remote Sens.*, vol. 45, no. 2, pp. 321–331, Feb. 2007.
[7] I. Cumming and F. Wong, *Digital Processing of Synthetic Aperture Radar Data*. Norwood, MA: Artech House, 2005.
[8] J. DiMarzio, A. Brenner, R. Schutz, C. Shuman, and H. Zwally, *GLAS/ICESat 500 m Laser Altimetry Digital Elevation Model of Antarctica*. Boulder, CO: Nat. Snow Ice Data Center, 2007. Digita media.
[9] R. M. Goldstein and C. L. Werner, "Radar interferogram filtering for geophysical applications," *Geophys. Res. Lett.*, vol. 25, no. 21, pp. 4035–4038, 1998.
[10] R. Hanssen, *Radar Interferometry, Data Interpretation and Error Analysis*. Norwell, MA: Kluwer, 2001.
[11] A. Hein, *Processing of SAR Data*. Berlin, Germany: Springer-Verlag, 2004.
[12] V. Helm, W. Rack, R. Cullen, P. Nienow, D. M. V. Parry, and D. Wingham, "Winter accumulation in the percolation zone of Greenland measured by airborne radar altimeter," *Geophys. Res. Lett.*, vol. 34, no. 6, p. L06 501, Mar. 2007. DOI: 10.1029/2006GL029185.
[13] P. Huybrechts, O. Rybak, F. Pattyn, U. Ruth, and D. Steinhage, "Ice thinning, upstream advection, and non-climatic biases for the upper 89% of the EDML ice core from a nested model of the Antarctic ice sheet," *Clim. Past*, vol. 3, no. 3, pp. 693–727, May 2007.
[14] I. Joughin, D. Winebrenner, M. Fahnestock, R. Kwok, and W. Krabill, "Measurements of ice-sheet topography using satellite radar interferometry," *J. Glaciol.*, vol. 42, no. 140, pp. 10–22, 2005.
[15] R. Kwok and M. Fahnestock, "Ice sheet motion and topography from radar interferometry," *IEEE Trans. Geosci. Remote Sens.*, vol. 34, no. 1, pp. 189–200, Jan. 1996.
[16] H. Liu, K. Jezek, B. Li, and Z. Zhao, *Radarsat Antarctic Mapping Project Digital Elevation Model Version 2*. Boulder, CO: Nat. Snow Ice Data Center, 2001. Digital media.
[17] J. Mohr, N. Reeh, and S. Madsen, "Three-dimensional glacial flow and surface elevation measured with radar interferometry," *Nature*, vol. 391, no. 6664, pp. 273–276, Jan. 1998.
[18] J. Mohr, N. Reeh, and S. Madsen, "Accuracy of three-dimensional glacier surface velocities derived from radar interferometry and ice-sounding radar measurements," *J. Glaciol.*, vol. 49, no. 165, pp. 201–209, Mar. 2003.
[19] E. Rignot, K. Echelmeyer, and W. B. Krabill, "Penetration depth of interferometric synthetic-aperture radar signals in snow and ice," *Geophys. Res. Lett.*, vol. 28, no. 18, pp. 3501–3504, 2001.
[20] P. A. Rosen, S. Hensley, H. A. Zebker, F. H. Webb, and E. J. Fielding, "Surface deformation and coherence measurements of Kilauea Volcano, Hawaii, from SIR C radar interferometry," *J. Geophys. Res.*, vol. 101, no. E10, pp. 23 109–23 125, 1996.
[21] R. Rosen, S. Hensley, I. Joughin, S. F. Li, E. Rodríguez, and R. Goldstein, "Synthetic aperture radar interferometry," *Proc. IEEE*, vol. 88, no. 3, pp. 333–382, Mar. 2000.
[22] G. Rotschky, W. Rack, W. Dierking, and H. Oerter, "Retrieving snowpack properties and accumulation estimates from combination of SAR and scatterometer measurements," *IEEE Trans. Geosci. Remote Sens.*, vol. 44, no. 4, pp. 943–956, Apr. 2006.
[23] H. Rott, K. Sturm, and H. Miller, "Active and passive microwave signatures of Antarctic firn by means of field measurements and satellite data," *Ann. Glaciol.*, vol. 17, pp. 337–343, 1993.
[24] C. Werner, U. Wegmüller, T. Strozzi, and A. Wiesmann, "Gamma SAR and interferometry software," in *Proc. 3rd ERS Symp. Space Service Environ.*, Florence, Italy, Mar. 1997.
[25] S. Williams, Y. Bock, and F. Peng, "Integrated satellite interferometry: Tropospheric noise, GPS estimates and implications for interferometric synthetic aperture radar products," *J. Geophys. Res.*, vol. 103, no. B11, pp. 27 051–27 068, Nov. 1998.
[26] H. J. Zwally, R. Schutz, C. Bentley, J. Bufton, T. Herring, J. Minster, J. Spinhirne, and R. Thomas, *GLAS/ICESat L2 Antarctic and Greenland Ice Sheet Altimetry Data V001*. Boulder, CO: Nat. Snow Ice Data Center, 2003. Digital media.
[27] H. J. Zwally, R. Schutz, C. Bentley, J. Bufton, T. Herring, J. Minster, J. Spinhirne, and R. Thomas, *GLAS/ICESat L2 Antarctic and Greenland Ice Sheet Altimetry Data V028*. Boulder, CO: Nat. Snow Ice Data Center, 2007. Digital media.

Reinhard Drews was born in Tübingen, Germany, in 1981. He received the Diploma degree in physics from the University of Bremen, Bremen, Germany, in 2007. He is currently working toward the Ph.D. degree at the Alfred Wegener Institute for Polar and Marine Research, Bremerhaven, Germany.

His research interest includes remote sensing of the cryosphere in relation to mass-balance studies, with a special focus on SAR interferometry combined with air- and ground-based ice-penetrating radar.

Wolfgang Rack (M'01) was borne in Graz, Austria, in 1968. He received the M.Sc. degree in meteorology and the Ph.D. degree in glaciology from the University of Innsbruck, Innsbruck, Austria, in 1995 and 2000, respectively.

From 2001 to 2006, he was a Research Scientist with the Alfred Wegener Institute for Polar and Marine Research, Bremerhaven, Germany. In 2006, he was appointed as a Senior Lecturer at the Gateway Antarctica—Center for Antarctic Studies and Research, University of Canterbury, Christchurch, New Zealand. His current research includes optical and microwave remote sensing studies of polar snow and ice from ground, air, and space. He actively contributed to several national and international projects on microwave signatures of snow, retreat, and breakup of ice shelves, glacier mass balance, and alpine hydrology. He has participated in several scientific expeditions to Antarctica, the Arctic, and Patagonia.

Christine Wesche was born in Halle, Germany, in 1981. She received the Diploma degree in geography from the Martin Luther University of Halle–Wittenberg, Halle, in 2005 and the Ph.D. degree in glaciology from the University of Bremen, Bremen, Germany, in 2009.

She is currently a Research Scientist with the Alfred Wegener Institute for Polar and Marine Research, Bremerhaven, Germany. Her research interests include ice sheet altimetry and tracking of icebergs using satellite images. She participated in an expedition to coastal Dronning Maud Land, Antarctica, in the beginning of 2007.

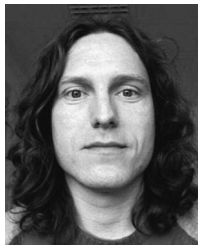

Veit Helm was born in Radebeul, Germany, in 1978. He received the Diploma degree in geophysics from the Technische Universität Bergakademie Freiberg, Freiberg, Germany, in 2003. He received the Ph.D. degree in glaciology from the University of Bremen, Bremen, Germany in 2009.

His research interests include remote sensing studies of snow and ice, with emphasis on LiDAR and radar SAR altimetry. He participated in several scientific expeditions to the Arctic and Antarctica.